Journal of Marine Research, 45, 293–318, 1987

Observations on the vertical structure of tidal and inertial currents in the central North Sea

by L. R. M. Maas[1] and J. J. M. van Haren[1]

ABSTRACT

Tidal and inertial current ellipses, measured at several locations and depths in the central North Sea during a number of monthly periods in 1980, 1981 and 1982, are decomposed into counterrotating, circular components to which Ekman dynamics are applied to determine Ekman layer depths and vertical phase differences, from which are inferred overall values of the eddy viscosity and drag coefficient. Stratification effects produce an additional vertical phase shift of the anticyclonic rotary component, indicative of an inverse proportionality of the eddy viscosity to the vertical density gradient. From the time variations of the Ekman layer depths of the semidiurnal tidal components, as well as from the vertical structure of the inertial current component, we infer variations in the relative vorticity of the low-frequency flow.

1. Introduction

The effects of bottom friction on a steady current in a rotating frame of reference (governed by Ekman dynamics, e.g. Pedlosky (1979)) and on an oscillating current in a resting frame (e.g. Lamb, 1975) bear similar features. Both show an amplitude decrease toward the bottom, accompanied by an anticyclonic veering with depth in the former case of a steady current and a phase advance toward the bottom in the latter situation of an oscillatory current (in the Northern hemisphere). Oscillatory currents (frequency σ) in a rotating frame should combine both aspects.

The nonviscous effect of rotation on an oscillating current is to yield a second, orthogonal velocity component producing an ellipsoidal motion in a horizontal plane exemplified by plane Sverdrup waves. The amplitude and phase of this extra velocity component introduce two more degrees of freedom, so that the ellipsoidal current motion is entirely described by four parameters:

- U maximum current velocity, or semi-major axis
- e eccentricity, i.e. the ratio of semi-minor (V) to semi-major axis, negative values indicating that the ellipse is traversed in an anticyclonic sense
- ψ inclination, or angle between east (x) direction and semi-major axis
- ϕ phase angle, i.e. the time of maximum velocity with respect to a chosen origin of time.

1. Netherlands Institute for Sea Research, P.O. Box 59, 1790 AB Texel, The Netherlands.

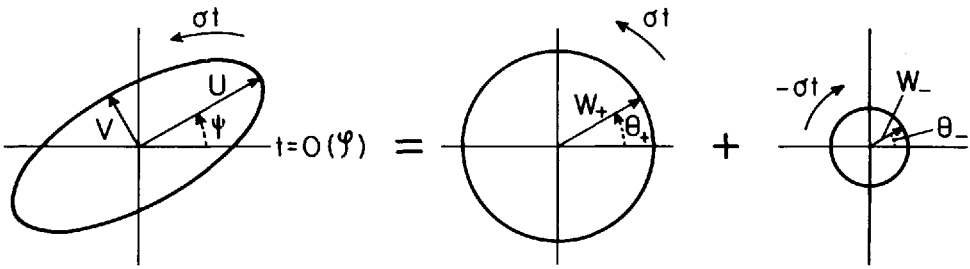

Figure 1. Decomposition of a tidal current ellipse (frequency σ), specified by the four ellipse parameters: magnitude of semi-major axis U, eccentricity $e = V/U$, (V: semi-minor axis), inclination ψ and phase angle ϕ, into two counterrotating currents of constant magnitudes $W_\pm$ and directions $\theta_\pm$.

Following Prandle (1982), to understand the vertical structure of these four parameters, we decompose the ellipsoidal motion into two counterrotating circular velocity components with fixed amplitudes (the radii $W_\pm$) and phases ($\theta_\pm$), Figure 1, in terms of which the ellipse parameters read

$$U = W_+ + W_-$$
$$e = (W_+ - W_-)/(W_+ + W_-)$$
$$\psi = (\theta_- + \theta_+)/2$$
$$\phi = (\theta_- - \theta_+)/2.$$

Sverdrup (1927) pointed out that, in terms of these rotary current parameters, the governing (linear) equations are solved in a straightforward way. It is conceptually advantageous, however, to stress that this solution procedure (Section 2) consists of two steps. Firstly, the circular velocity components, which themselves are given on a uniformly rotating f-plane, are transformed to two co-rotating frames having different angular velocities $\nu/2 = (f \pm \sigma)/2$, where f denotes the local inertial frequency. Secondly, since in their respective co-rotating frames the velocity vectors reduce to steady currents, merely giving the amplitude and angle with respect to an originally chosen direction, Ekman dynamics can be applied directly. This explicit separation allows us to obtain a qualitative mental picture of the causal relations underlying the vertical structure of the ellipse parameters.

Thus, for super inertial frequencies ($\sigma > f$) the net rotation sense of the frame co-rotating with the anticyclonic current component is negative (clockwise). Hence, dynamics apply as if we are on the Southern hemisphere, and therefore the anticyclonic velocity vector will rotate clockwise toward the bottom. For semidiurnal frequencies at moderate latitudes ($\sigma \gtrsim f$) a separation of Ekman layer scales, $\delta_\pm = \sqrt{2K/|f \pm \sigma|}$, (Soulsby, 1983) is predicted: $\delta_+ \ll \delta_-$. Here K denotes the turbulent eddy viscosity. Near the bottom, therefore, the cyclonic current component will be less reduced than

its anticyclonic counterpart. This implies that a near-surface rectilinear current acquires an elliptical shape, traversed in a cyclonic sense, closer to the bottom.

For subinertial frequencies ($\sigma < f$) the net rotation sense of both co-rotating frames is positive (anticlockwise), hence currents will rotate anticlockwise toward the bottom for both components, although (for the same reason as above) there may be a distinct difference in scales between them.

The anticyclonic component of the inertial oscillations ($\sigma = f$) is by its nature given in a nonrotating frame. Inspection of the governing equations predicts some sort of a z^2-profile due to bottom friction (where z is the vertical distance above the sea bed) and the absence of any turning with depth.

2. Theory

The equations of motion describing the dynamics of tides in a homogeneous sea in the presence of turbulent friction read (nondimensionally) (Sverdrup, 1927):

$$\frac{\partial u}{\partial t} - v + \frac{\partial \zeta}{\partial x} = \frac{E}{2}\frac{\partial^2 u}{\partial z^2} \tag{1a}$$

$$\frac{\partial v}{\partial t} + u + \frac{\partial \zeta}{\partial y} = \frac{E}{2}\frac{\partial^2 v}{\partial z^2} \tag{1b}$$

$$\frac{\partial \zeta}{\partial t} + \nabla \cdot \left(\int_0^1 \mathbf{u}\, dz \right) = 0 \tag{1c}$$

$$\frac{\partial \mathbf{u}}{\partial z} = s \cdot \mathbf{u} \quad \text{at} \quad z = 0 \tag{1d}$$

$$\frac{\partial \mathbf{u}}{\partial z} = 0 \quad \text{at} \quad z = 1. \tag{1e}$$

The vertical coordinate, z, measured upward from the top of the bottom boundary layer is scaled with the local depth H. Horizontal coordinates, x and y, corresponding to east and north directions, are scaled with the barotropic Rossby deformation radius $R = \sqrt{gH}/f$, where g denotes the acceleration of gravity. Time t is scaled with f^{-1}. Horizontal velocities u and v, corresponding to currents in x and y directions, are scaled with a typical velocity magnitude $[u]$. The surface elevation ζ is nondimensionalized with $[u]/\sqrt{gH} \times H$. The only two remaining nondimensional parameters are the familiar Ekman number $E = 2K/fH^2$, and the stress parameter $s = rH/K$, with r a bottom friction velocity ($r = \mathrm{O}(10^{-4}\mathrm{m\ s^{-1}})$; Csanady, 1982) related to the drag coefficient C_d ($C_d = 2 - 4 \times 10^{-3}$; Bowden, 1983). The stress parameter varies between no-stress ($s \to 0$) and no-slip i.e. 'infinite' stress ($s \to \infty$), when the flow sticks completely to the bottom. The bottom boundary condition (1d) is derived at the top of

the bottom boundary layer ($z = 0$), circumventing a detailed description of this shallow boundary layer of approximately 1 m depth (Bowden, 1983), by equating interior stress, $K\,\partial \mathbf{u}/\partial z$, to bottom stress, $C_d|\mathbf{u}|\mathbf{u}$, or more preferably, its linearized counterpart $r\mathbf{u}$. The connection between r and C_d can be established by an energy criterion, requiring the dissipation averaged over a tidal cycle to be equal (Lorentz, 1926), and gives $r = 8/3\pi \times C_d U(0)$, where $U(0)$ denotes the tidal current amplitude at the bottom. The correct spatial and temporal dependence of the eddy viscosity "constant" K is an intensively studied subject in the tidal context (Tee, 1979; Prandle, 1982; Fang and Ichiye, 1983). Since in this paper, the diffusion process is studied over large spatial areas from observations taken over monthly periods in different years, the parameterization should lose its sensitivity to the detailed structure of the flow field and a constant eddy viscosity is therefore adopted.

By assuming $u = R1(\tilde{u} \exp(-i\sigma' t))$, where $\sigma' = \sigma/f$, $\tilde{u} = U(x) \cdot \exp(i\phi_u(x))$, and similarly for v and ζ, we may obtain two independent second order differential equations by forming the complex velocities

$$w_- = \frac{\tilde{u} + i\tilde{v}}{2} = W_- \exp(i\theta_-)$$

$$w_+ = \frac{\tilde{u} - i\tilde{v}}{2} = W_+ \exp(-i\theta_+) \tag{2}$$

related to the ellipse parameters discussed in the introduction. These velocities, w_- and w_+, act as the amplitudes of the circular rotary current components, which traverse the unit circle in an anticyclonic and cyclonic sense, respectively, as can be seen when we combine the horizontal velocities u and v directly into a complex velocity w:

$$w = u + iv = U\cos(\phi_u - \sigma' t) + iV\cos(\phi_v - \sigma' t)$$
$$= w_- \exp(-i\sigma' t) + w_+^* \exp(i\sigma' t), \tag{3}$$

where the asterisk, $(\,)^*$ denotes a complex conjugate. In terms of these velocities the equations of motion (1a, b) become, omitting the common factor $\exp(\pm i\sigma' t)$:

$$i(1 - \sigma')w_- + \frac{1}{2}\nabla\zeta = \frac{E}{2}\frac{d^2 w_-}{dz^2}, \quad -i(1 + \sigma')w_+ + \frac{1}{2}\nabla^*\zeta = \frac{E}{2}\frac{d^2 w_+}{dz^2} \tag{4}$$

with boundary conditions

$$\frac{dw_\pm}{dz} = s w_\pm \qquad \text{at } z = 0$$

$$\frac{dw_\pm}{dz} = 0 \qquad \text{at } z = 1 \tag{5}$$

where

$$\nabla = \frac{\partial}{\partial x} + i\frac{\partial}{\partial y} \text{ and } \nabla^* = \frac{\partial}{\partial x} - i\frac{\partial}{\partial y}.$$

These equations are equivalent to the (complex) equation describing the dynamics of a steady current on a plane uniformly rotating at a rate $\nu/2$ (Ekman dynamics; Pedlosky, 1979):

$$iw + \nabla p = \frac{E_\nu}{2}\frac{d^2w}{dz^2} \tag{6}$$

with

$$\frac{dw}{dz} = sw \qquad \text{at } z = 0 \tag{7a}$$

$$\frac{dw}{dz} = 0 \qquad \text{at } z = 1 \tag{7b}$$

when replacing the Ekman number $E_\nu = 2K/\nu H^2$ by either $E/(1 - \sigma')$, or $-E/(1 + \sigma')$ and the pressure gradient ∇p by either $\frac{1}{2}\nabla\zeta/(1 - \sigma')$, or $-\frac{1}{2}\nabla^*\zeta/(1 + \sigma')$ respectively. The unconventional choice of the inertial frequency, ν, has been adopted to allow for a direct application to frames rotating with rates $(f \pm \sigma)/2$.

The mathematical equivalence of the dynamics governing the rotary components (4) to those that govern a steady current (6) implies the underlying transformation to co-rotating co-ordinate frames. Borrowing the Ekman solutions to (6) (with a modified bottom stress condition, (7a)),

$$w = \overline{w}\left(1 - \frac{\cosh \alpha z}{\cosh \alpha + (\alpha/s)\sinh \alpha}\right) \tag{8}$$

where

$$\overline{w} = i\nabla p, \qquad \alpha = (1 + i)/E_\nu^{1/2} \tag{9}$$

we obtain the solutions of (4–5) as:

$$w_\pm = \overline{w}_\pm\left(1 - \frac{\cosh \alpha_\pm z}{\cosh \alpha_\pm + (\alpha_\pm/s)\sinh \alpha_\pm}\right) \tag{10}$$

where

$$\overline{w}_- = \tfrac{1}{2}i\nabla\zeta/(1 - \sigma'), \qquad \overline{w}_+ = -\tfrac{1}{2}i\nabla^*\zeta/(1 + \sigma') \tag{11}$$

and

$$\alpha_- = \begin{cases} (1 - i) \cdot (H/\delta_-) & \sigma' > 1 \\ (1 + i) \cdot (H/\delta_-) & 1 > \sigma' \end{cases}$$

$$\alpha_+ = \begin{cases} (1 - i) \cdot (H/\delta_+) & \sigma' > -1 \\ (1 + i) \cdot (H/\delta_+) & -1 > \sigma' \end{cases} \tag{12}$$

in terms of Ekman layer depths (Soulsby, 1983)

$$\delta_\pm = \sqrt{2K/(|f \pm \sigma|)}. \tag{13}$$

Solutions (10), finally, are used in the comparison to the observed profiles in Section 4. Their qualitative features are discussed in the introduction.

3. The data acquisition

During the spring, summer and autumn of 1980, 1981 and 1982 a collaborative study was performed in the stratified central North Sea by the Royal Netherlands Meteorological Institute (KNMI), the Institute of Meteorology and Oceanography Utrecht (IMOU) and the Netherlands Institute for Sea Research (NIOZ). In Figure 2, local bathymetry and current meter mooring positions are shown. Table 1 gives the precise operational periods and depths. The current meter records were supplemented with extensive hydrographic surveys on both large (O(100 km)) and small (O(20 km)) horizontal scales. A limited number of thermistor chains and pressure gauges completed the data equipment. Onset, evolution and decay of the stratification (van Aken, 1984, 1986) and frontal dynamics (van Aken *et al.*, 1987), have been discussed elsewhere.

The current measurements presented here were performed in both stratified and well-mixed periods. Local water depths, H, are between 45 and 50 m, the measurement site being a relatively flat area. Each of the time series of current measurements has been harmonically analyzed using a small number of well separated tidal frequencies (O_1, K_1, N_2, M_2, S_2, M_4, M_6) and the inertial frequency f (Dronkers, 1964). In view of the presence of stratification some internal tide contamination may be anticipated. Since the observation site is far away from any topographic features we assume that free internal tides will not be phaselocked to the surface tide and hence, in view of the large periods used, will be filtered out due to their intermittent character (Wunsch, 1975).

Since small depth differences at different moorings result in local differences in tidal amplitudes, the current measurements were normalized by their weighted, depth-averaged values (the weighting factor of a current meter being proportional to the depth increment which it represents, divided by water depth), while phases were taken with respect to those from the current meter near the surface.

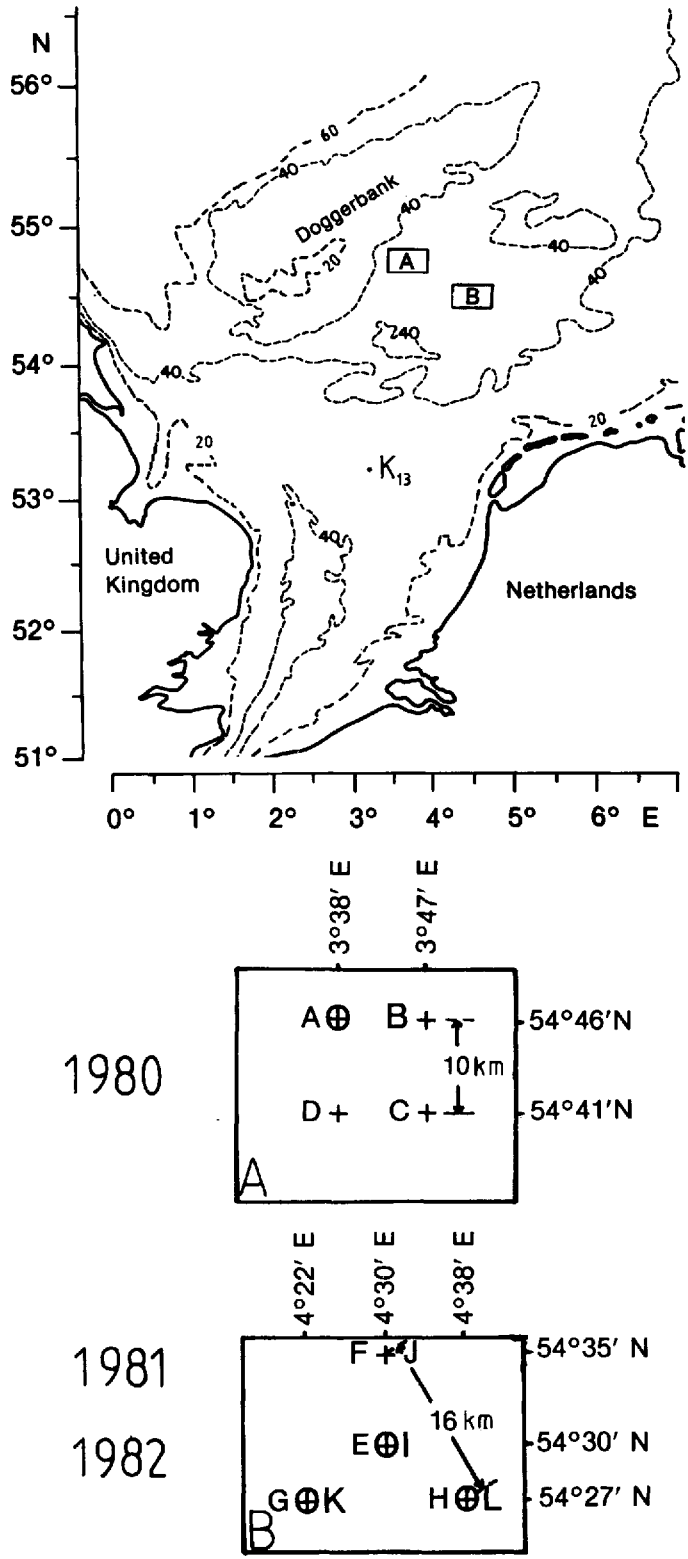

Figure 2. (a) Map of part of the North Sea with the positions of mooring networks in 1980 (A) and 1981, 1982 (B), with isobaths in m. Wind observations are performed at platform labelled K13. (b) Mooring configurations in 1980, 1981 and 1982. Current meters are denoted by +, thermistor chains by 0.

Table 1. Positions, current meter depths, local sea depth and operational periods of the current measurements in 1980–1982.

Station	N	E	Depths (m)	Water depth (m)	Period (year-day)	Year
A	54°46′	3°38′	16	46	240–289	1980
			41		240–275	
B	54°46′	3°47′	14	46	240–305	
			28, 41		240–275	
C	54°41′	3°47′	13	46	240–275	
			41		240–273	
D	54°41′	3°38′	27	46	240–273	
			41		240–274	
E	54°30′	4°30′	13, 19, 31, 38, 45	50	133–155	1981
F	54°35′	4°31′	13, 29, 45	50	133–155	
G*	54°27′	4°22′	13, 29, 45*	50	133–155	
H	54°28′	4°38′	12, 28, 42	47	133–155	
I	54°30′	4°30′	12, 24, 30, 37	49	215–252	1982
			18		215–239	
			44		215–240	
J	54°35′	4°30′	12, 43	48	215–252	
K	54°27′	4°22′	12, 27, 44	49	215–252	
L	54°27′	4°38′	12, 27, 42	47	215–252	

*The bottom current meter at G, 1981 was eliminated due to compass failure.

4. Observational versus theoretical current profiles

a. The superinertial tidal frequency band

Bottom friction imposes a number of typical features on the vertical structure of the tidal currents, as demonstrated in Figure 3 for the observed M_2 component at position I (Table 1). From the surface downward we observe:

— a slight increase in maximum current amplitude followed by a sharp decrease toward the bottom;

— a clockwise turning of the major axis;

— an increase in the eccentricity of the ellipse;

— a phase advance, indicating that maximum current speeds are reached earlier near the bottom.

These features, summarized here for a single span of time at a specific geographic position, are directly visible for all observational periods and positions listed in Table 1 from graphs showing the ellipse parameters versus depth, which are plotted in Figure 4, for the M_2 frequency. Transforming these ellipse parameters to amplitudes and phases of the rotary, circular components confirms experimentally the expected

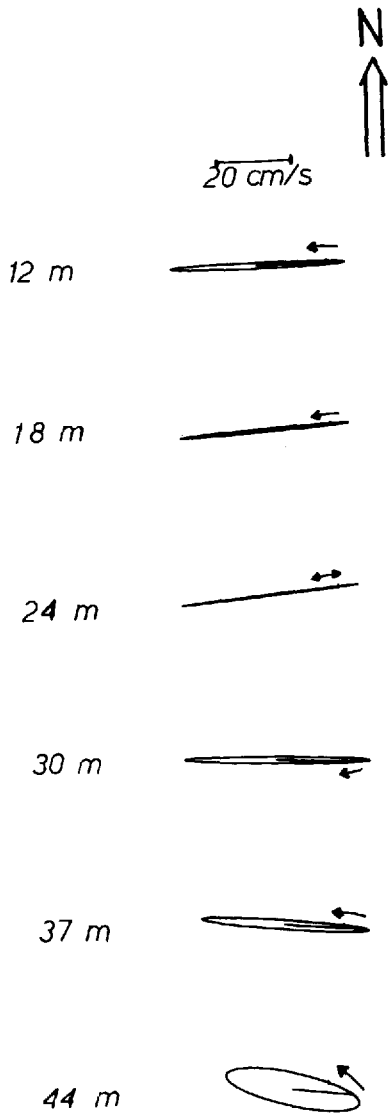

Figure 3. Observed M_2-current ellipses at position I (Fig. 2) in 1982 for the period listed in Table 1 as a function of depth. The angle which each straight line makes with true North gives the phase angle ϕ with respect to the beginning of the year of observation.

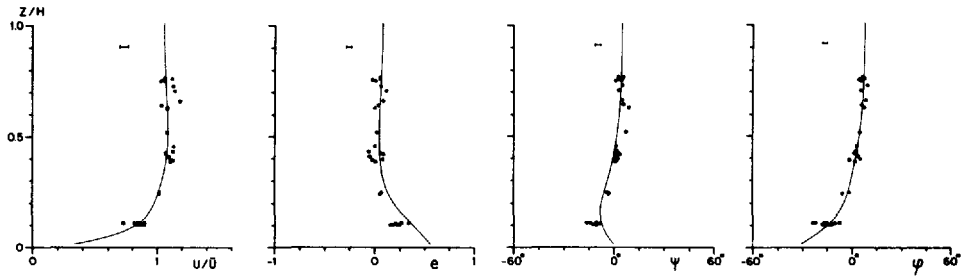

Figure 4. Observations (denoted by dots) of ellipse parameters for the M_2-frequency versus normalized depth. Maximum current (U) is divided by $\bar{U}$, the weighted depth averaged current amplitude. Phases are given with respect to their surface values. Solid curves are best fit theoretical curves as derived in Section 2. Error bars are indicated at the top.

separation of vertical friction scales (Fig. 5). Phases turn in opposite directions toward the bottom, in agreement with predictions from Ekman dynamics, for frames rotating in opposite directions.

The theoretical curves, (10), are given by the solid lines in Figures 4 and 5. The magnitude of the constants E and s, required in (10), have been determined experimentally by choosing a best fit by face value of the theoretical curves to the observations. Note that this best fit determination has to be done simultaneously for each set of four graphs in Figures 4 and 5. The experimental values are $E = (1.0 \pm 0.1) \times 10^{-2}$ and $s = 10 \pm 1$, from which we deduce, for a depth $H = 48$ m, an experimental value of $K = (1.4 \pm 0.1) \times 10^{-3} \text{m}^2\ \text{s}^{-1}$ and $r = (2.9 \pm 0.2) \times 10^{-4}\ \text{m s}^{-1}$. From the theoretical profile (10) we find a time-averaged bottom velocity magnitude: $U(0)$ of 0.55 times a vertically averaged tidal velocity amplitude of 25 cm s^{-1}. This results in $C_d = (2.5 \pm 0.2) \times 10^{-3}$. This value of the drag coefficient agrees with a typical value (Bowden, 1983), although the friction velocity r is a little less than suggested by Csanady (1982). The value of the eddy viscosity K falls below theoretical estimates of $K = k_E u_*/20f$ (where the friction velocity $u_* = C_d^{1/2}\, U(0)$) appropriate for

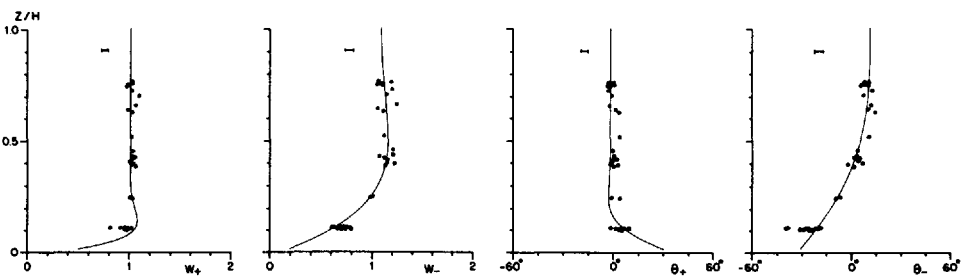

Figure 5. Observations (denoted by dots) of amplitudes $W_\pm$ and phase angles $\theta_\pm$ of the M_2 frequency rotary current components as a function of normalized depth. Solid curves are best fit theoretical curves. Error bars are indicated at the top.

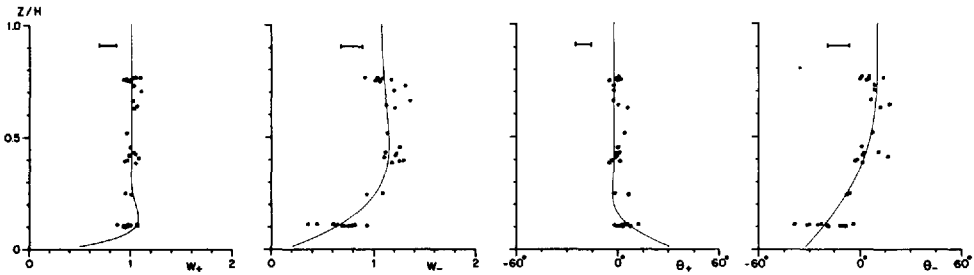

Figure 6. As Figure 5 but for the S_2 frequency.

situations where $k_E u_*/f < H$ (Csanady, 1976). There is some uncertainty about the value of the constant k_E, which varies between 0.1 (Csanady, 1976) and the von Karman constant 0.4 (Wimbush and Munk, 1970). With $k_E = 0.1$ we obtain an estimated $K = 1.6 \times 10^{-3}$ m^2 s^{-1}. An inferred boundary layer thickness (a weighted combination of the two Ekman depths $\delta_\pm$) is below 20 m and in this sense agrees with values given by a map of this parameter by Soulsby (1983) at our mooring location.

Finally, the value of the nondimensional stress parameter $s \gg 1$ indicates that the no-slip Ekman boundary condition is 'more appropriate' than a no-stress condition.

The most important deviations between observed and theoretical ellipse parameter values occur at the bottom current meter and may be due to either an incorrect depth determination (probably less than 0.5 m), to which the sheared current profile is particularly sensitive near the bottom, or a local breakdown of the constant K assumption, which, according to Prandle (1982), should be replaced by an eddy viscosity increasing from the bottom upward, recognizing the increase in mixing-length.

Errors in the observed ellipse parameters, denoted by error bars, were estimated, using Tee's (1982) method, with an overall root-mean-square value of the residual currents (defined as original minus harmonic time series) of $u' = 5$ cm s^{-1}. This value implies an overall error in the estimated harmonic amplitude of the Cartesian velocity components of $\triangle = u'/M^{1/2} = 0.25$ cm s^{-1}, where M denotes half the number of hourly data points (typically $M = 400$, Table 1). The errors in the ellipse parameters are inversely proportional to the amplitudes of the appropriate counterrotating current components.

The behavior of the vertical profiles of other semidiurnal frequencies (S_2 and N_2) is similar to that of the M_2 components (Figs. 6 and 7). Their smaller energetic content ($S_2 = O(7$ cm s$^{-1})$, $N_2 = O(4$ cm s$^{-1})$) is reflected in a larger scatter around the mean profiles. This scatter tends to be larger for the anticyclonic component, despite the fact that the energy is fairly well distributed over the two rotary components (for S_2, $\overline{W}_+ = 3.9$ cm s^{-1}, $\overline{W}_- = 3.2$ cm s^{-1}, while for N_2, $\overline{W}_+ = 2.3$ cm s^{-1}, $\overline{W}_- = 2.0$ cm s^{-1}). This is probably due to a larger influence of stratification effects on the anticyclonic component, as will be examined in the next subsection for M_2. The theoretical curves

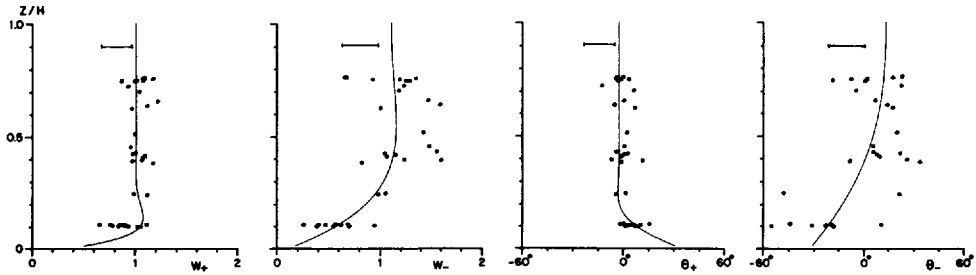

Figure 7. As Figure 5 but for the N_2 frequency.

used in these figures are determined by using the best fit parameter values obtained from the M_2-fit and confirm their application to these frequencies too. The difference, caused by a changing frequency, is, as expected, small and curves for M_2, S_2 and N_2 are nearly indistinguishable, implying that friction operates in a similar way in this semidiurnal band.

Theoretically there is a difference with the profiles calculated for the M_4 frequency. Observed amplitudes, however, are small ($\overline{W}_+ = 0.54$ cm s^{-1}, $\overline{W}_- = 0.54$ cm s^{-1}) (Fig. 8) and one must be cautious in drawing conclusions. The calculated error bars exceed any variance suggested by the observations by a factor two. This implies that the noise level is smaller in this frequency range, and therefore the noise is probably not white, as the theoretical estimate (Tee, 1982) assumes.

Dependence of eddy viscosity on stratification. For the M_2 frequency the high signal-to-noise ratio makes it worthwhile examining the deviations from the theoretical curves (Figs. 4 and 5), which we believe to be related to stratification effects.

In August–September 1982 this could be checked since a frontal passage was recorded separating a period (day 215–230) with a well-defined thermocline (temperature jump 9°C) at about 25 m depth, from a weakly stratified period (day 237–252), where the thermocline (temperature difference 3°C) was at some 40 m depth. The low-passed temperature field at the central mooring I (Fig. 9a, van Aken *et al.*, 1987)

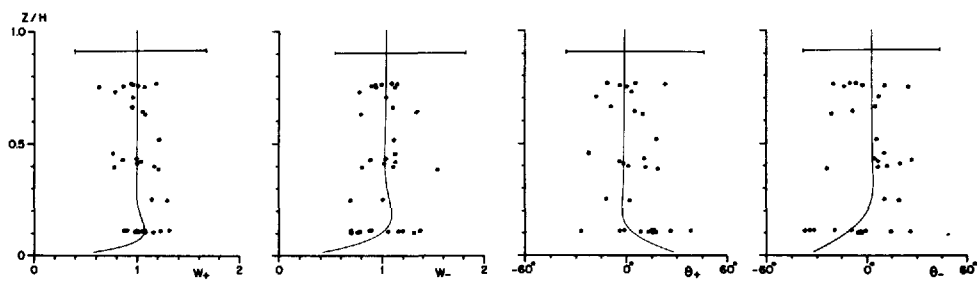

Figure 8. As Figure 5 but for the M_4 frequency.

Figure 9. (a) The low-passed temperature field at mooring I (1982). Isotherms are given in °C. (From Van Aken *et al.*, 1987). (b) Observed windstress ($\sim C_d|\mathbf{u}_a|\mathbf{u}_a$), using the oceanographic convention, at platform K13 (Fig. 2).

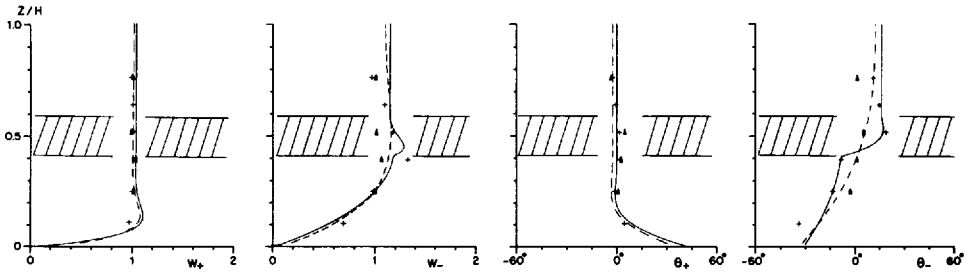

Figure 10. Observed counterrotating M_2-tidal velocity components for the stratified (day 215–230; +) and unstratified (day 237–252; △) periods (Fig. 9). The solid line gives the analytical result of a three-layer model with a small eddy viscosity value, $K = 6 \times 10^{-4}\ m^2\ s^{-1}$, in the middle layer. These curves may be compared with the original curves from Figure 5, dashed here. The hatched area represents the modelled thermocline.

is interpreted from hydrographic surveys as a gradual deepening of the surface mixed layer (day 215–230) due to wind-mixing (Fig. 9b), followed by a subsequent period (day 230–238) of combined wind-mixing and frontal advection. In Figure 10 we contrast results from a harmonic analysis of the two periods. Note that the observations for the "unstratified" period (day 237–252) are biased by the absence of the bottom current meter information from day 240 onward. Free internal tide motions can be excluded as being the source of the observed deviations since horizontal coherence analysis of the residual signals (defined as original minus tidal harmonic time series) showed very small phase differences between the different moorings ($\lesssim 20°$), which is at variance with a theoretically expected value of approximately 180° for the given stratification and mooring distances (Schott, 1977).

Figure 10 shows that deviations from the theoretical curves in Figure 5 (dashed here) occur in the anticyclonic component only. The inference is that the cyclonic Ekman layer depth is so small that the bottom Ekman layer is well separated from the Ekman layer at the pycnocline. In contrast, the anticyclonic Ekman layers from bottom, interface and (possibly) surface apparently interact.

A density jump, such as that occurring during the "stratified" period, is believed to suppress turbulent motions within the pycnocline, inhibiting momentum transfer and resulting in a slab layer motion. Following Fjeldstad (1963), it is appropriate to model the eddy viscosity in inverse proportion to the density gradient. To idealize the geometry we consider a three-layer viscous model in which the eddy viscosity in the middle layer is an order of magnitude less than that of the homogeneous bottom and surface layers (Sverdrup, 1927). For simplicity, we assume the eddy viscosity in the latter layers to be equal. The equations of motion in each of the layers are equivalent to (4), subsequently applied to frames rotating with the anticyclonic and cyclonic components, implying that $E_{j-} = E_j/(\sigma' - 1) \simeq 5 \times E_j$; $E_{j+} = E_j/(\sigma' + 1) \simeq 0.5 \times E_j$ ($j = 1, 2, 3$) for $\sigma' \simeq 1.2$. Requiring velocity and stress continuity at the bottom and top

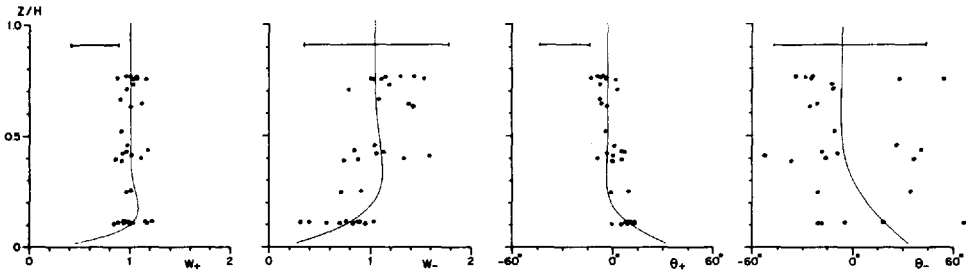

Figure 11. As Figure 5 but for the O_1 frequency.

of the interior layer one may find the analytical solution of the current profiles drawn in Figure 10. For convenience, we adopted a no-slip bottom and stress-free surface boundary condition. The best fit values of the Ekman numbers, determined again by face value, are $E_1 = E_3 = 1.5 \times 10^{-2}$ and $E_2 = 5 \times 10^{-4}$, setting the middle layer thickness equal to 0.18 close to the observed pycnocline thickness.

The resulting calculated phase jump of approximately 30° for θ_- at the bottom of the interior layer is in accordance with the observed phase jump, thus confirming the likeliness of a reduced eddy viscosity value in stratified circumstances, as has been verified from other data sets (e.g. Gargett and Holloway, 1984).

The amplitude profiles generally correspond well to the observations, but fail to describe the amplitude decrease in the anticyclonic component toward the surface. This is probably due to a failure in the applied zero surface stress condition, since in general it reads $\tau = K\,\partial\mathbf{u}/\partial z = C_d|\mathbf{u}_a - \mathbf{u}|(\mathbf{u}_a - \mathbf{u})$, where $\mathbf{u}_a$ is the velocity of the air, which under calm weather conditions ($\mathbf{u}_a \ll \mathbf{u}$), reduces to $K\,\partial\mathbf{u}/\partial z = -C_d|\mathbf{u}|\mathbf{u}$. This may, again, be linearized, as for the bottom stress condition, to $\partial\mathbf{u}/\partial z = -\gamma\mathbf{u}$ with γ a nondimensional surface stress parameter, which we took to be zero up to here. Note that since we are looking at the current profile $\mathbf{u}$ of one specific tidal component, the wind speed $\mathbf{u}_a$ also refers to the contribution of the wind in this frequency range only, giving some wider range of applicability to the "calm weather" condition. Applying the latter surface stress condition, qualitative agreement in amplitude decrease is obtained for $\gamma = 1$. This both shows that the wind has little persistent influence on the M_2-tide and that surface friction may not always be negligible.

The observed values of the surface and bottom stress parameters allow the determination of typical stress magnitudes, using a velocity magnitude of O(10 cm s^{-1}) $\tau_{\text{surface}} = 0.02$ dyn cm^{-2} and $\tau_{\text{bottom}} = 0.2$ dyn cm^{-2} (compare with a typical surface wind stress $\tau = 2$ dyn cm^{-2} based on $\mathbf{u}_a = 10$ m s^{-1}).

b. The subinertial tidal frequency band

Observed and theoretical profiles for the diurnal constituents O_1 and K_1 are given in Figures 11 and 12.

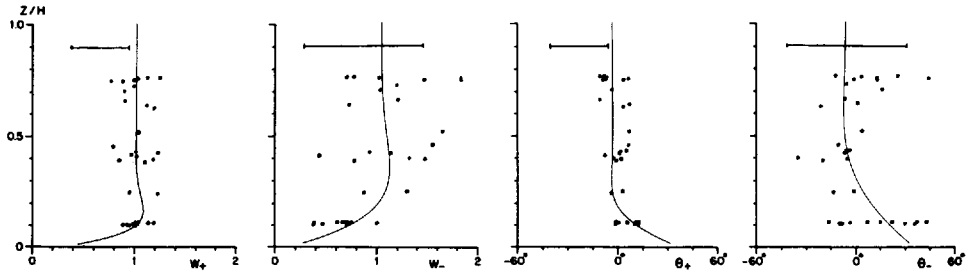

Figure 12. As Figure 5 but for the K_1 frequency.

In both co-rotating frames, the theoretically expected cyclonic rotation of the current vectors toward the bottom is more or less confirmed at both subinertial frequencies, although the observations can hardly be used to support the predicted ratio of friction depths $\delta_+/\delta_- = \sqrt{(f+\sigma)/(f-\sigma)} = 0.4$. Both diurnal components are rotating predominantly cyclonic with time; for O_1, $\overline{W}_+ = 1.4$ cm s^{-1} and $\overline{W}_- = 0.5$ cm s^{-1}, while for K_1, $\overline{W}_+ = 1.2$ cm s^{-1} and $\overline{W}_- = 0.6$ cm s^{-1}, hence the large scatter in the anticyclonic components.

Note that the theoretical curves have again been calculated using the parameter values $E = 0.01$ and $s = 10$ obtained from the M_2 fit, which seem to be fairly suitable.

c. Inertial oscillations

The observed tidal current components do not show the influence of stratification except for the effects on K, treated in Section 4a. The observed inertial oscillations are an exception at this point and seem to be purely baroclinic in nature. In Figure 13 this difference is demonstrated for observations in May 1981, with a mean thermocline depth at 15 m. For mooring E the current ellipses are drawn resulting from harmonic analyses for O_1, f and S_2 (with different scaling) respectively. The 180° phaseshift in f between the current ellipse near the surface and the lower four current ellipses clearly indicates the presence of first mode, baroclinic inertial motion. The inertial current ellipses are almost circular, rotating in an anticyclonic sense in time. This reflects the resonant response with which the anticyclonic inertial oscillations react to a broad frequency band wind forcing (Pollard and Millard, 1970). This inertial oscillation was also present at the other three moorings in 1981, showing marginal phase shifts between current meters at comparable depths. A harmonic analysis was performed for the current meter records in 1982 for both the "stratified" and "unstratified" period. Figure 14 demonstrates the dramatic decrease in amplitude of the internal, inertial oscillation in the second "unstratified" period, despite the fact that the wind forcing is not significantly less than over the "stratified" period (Fig. 9b).

The 1982 observations (Fig. 14) demonstrate more clearly than those of 1981 (Fig. 13) the influence of bottom friction which causes a strong reduction in amplitude

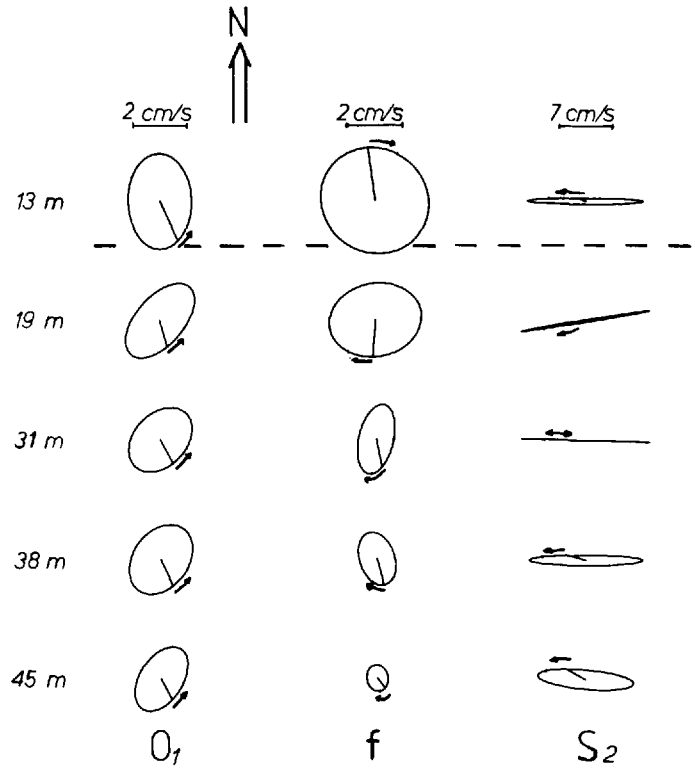

Figure 13. Observed current ellipses for O_1, f and S_2 at position E for the period in 1981 listed in Table 1, as a function of depth. The phase angles ϕ with respect to true North are given by a straight line. Note the differences in scales. The depth of the thermocline is indicated by a dashed line.

toward the bottom, together with a phase lead indicative of downward energy propagation (Gill, 1984).

In Figure 15 we have plotted the observed (dominant) anticyclonic inertial amplitudes and phases for the 1982 data as a function of depth. The net rotation rate of the frame $\nu/2 = (f - \sigma)/2$ approaches zero. In this limit the velocity profile w_-, from (10), approaches with $\nu' = 1 - \sigma'$:

$$\lim_{\nu' \to 0} w_- = \frac{\nabla\zeta}{2E} z(z-2)\left\{1 + \frac{i\nu'}{6E}(z^2 - 2z - 4)\right\} + O(\nu'^2) \qquad (14)$$

for the more transparent no-slip bottom boundary condition ($s \to \infty$). Thus, a barotropic inertial wave acquires a z^2-structure. Clearly, the observations imply that the inertial wave mode is of a baroclinic, rather than barotropic nature. Hence, if the density structure is modelled with a profile linearly increasing downward, the pressure gradients may also have a vertical structure imposed by any one of the internal modes:

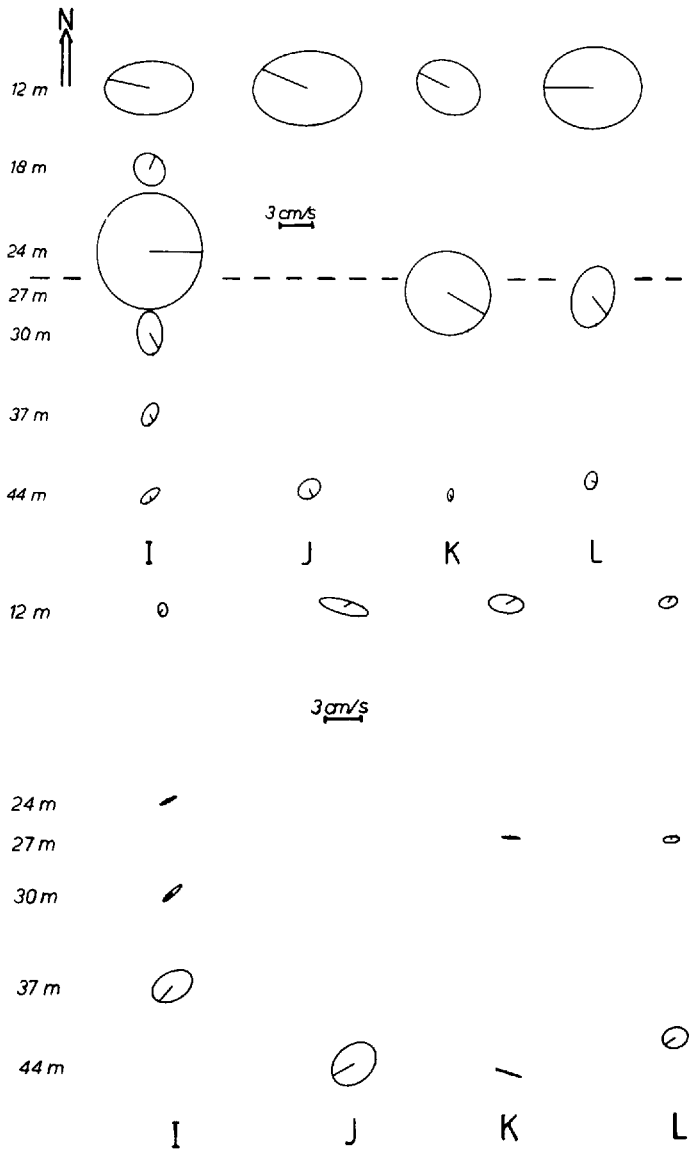

Figure 14. Observed current ellipses as a function of depth for inertial frequency motion during the stratified (a) and unstratified (b) periods in 1982. Phase angles ϕ with respect to true North are given by the straight lines. The depth of the thermocline in the stratified period is indicated by a dashed line.

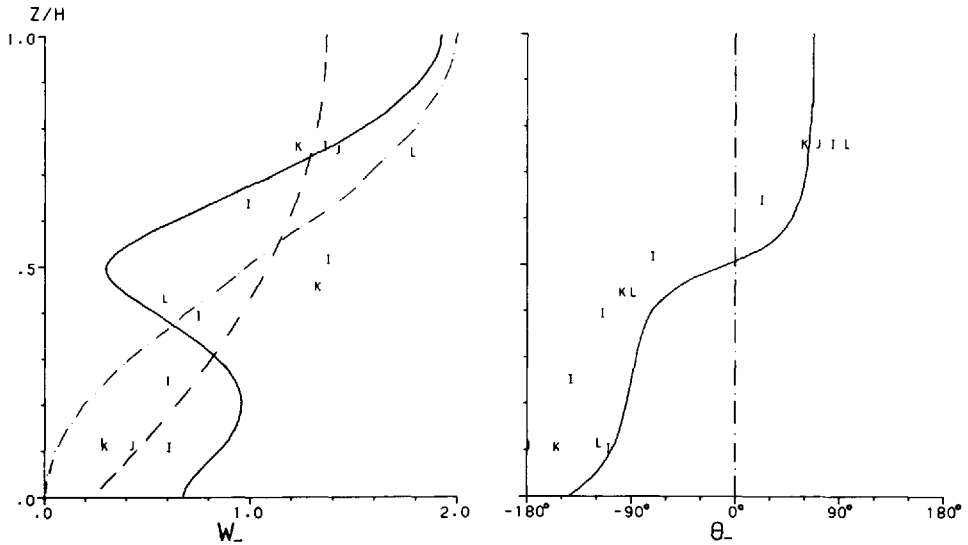

Figure 15. As Figure 5 for the anticyclonic inertial current components in 1982. Theoretical barotropic (dashed) and first mode baroclinic (dashed-dotted) profiles correspond to (14) and (15), Section 4c, respectively. The solid curve represents a first mode, baroclinic profile obtained with an apparent Ekman number, $E_\nu = 2K/\nu H^2 = 0.1$ and stress parameter $s = 10$.

$\nabla\zeta \cdot \cos n\pi z$ (Wunsch, 1975). In particular a first mode internal wave gives, again in the no-slip limit, for vanishing frame rotation rates

$$\lim_{\nu' \to 0} w_- = \frac{\nabla\zeta}{\pi^2 E}\left\{\sin^2\frac{\pi}{2}z + \frac{i\nu'}{E}z(z-2)\right\} + O(\nu'^2). \tag{15}$$

Neither of these profiles seem to offer a sufficient description (Fig. 15). Note that they especially predict a zero phaseshift in the vertical. The reason for this bad fit is that modification of a baroclinic current is very sensitive to deviations of the frequency from f, because the apparent Ekman number $E_\nu = E \cdot f/\nu$ multiplies the large parameter f/ν with the Ekman number $E = 2K/fH^2$, which itself is a small number of $O(10^{-2})$ (Section 4a). Therefore, slight deviations of ν, away from zero, of $O(10^{-1} \times f)$ may give rise to small values of the apparent Ekman number E_ν instead of leading to an infinite E_ν, which formally applies in the limit $\sigma \to f$ ($\nu' \to 0$) considered above. With $E_\nu = O(10^{-1})$ a qualitative agreement is, indeed, obtained between the observations and a frictionally modified, first mode baroclinic wave in a linearly stratified sea (the solid curve in Fig. 15), pointing at the presence of low-frequency relative vorticity. The crudeness of the adopted model of the density profile demonstrates that no more than qualitative agreement is pursued here. However, the model confirms the observed rotation of the anticyclonic current vector of about 220° toward the bottom, which adds

Table 2. Amplitudes and phases of 'surface' current meters for the inertial frequency at moorings in 1982.

Position (1982)	W_+ (cm/s)	W_- (cm/s)	θ_+	θ_-
I	0.5	1.8	27°	−18°
J	0.6	2.3	71°	−31°
K	0.2	1.8	−11°	−43°
L	0.2	2.5	15°	−7°

the frictional effect of some 40° to the 180° phase jump of a first mode baroclinic wave.

The relatively small phase differences at comparable depths between the four moorings (Table 2) (for the anticyclonic component less than 40°) indicate that there is a strong coherence between the time series and that the wavelength of the inertial wave greatly exceeds the mooring separation distance of O(10 km). This is in accordance with results found by Schott (1971), who estimated a wavelength of O(50 km) for an area just north of the Dogger Bank. The propagation direction suggested by the phase values in Table 2 is east-south-east and points to the Dogger Bank as source area, as in Schott's study.

That inertial oscillations can be captured with a sharp spectral filter like harmonic analysis indicates the persistence of these motions, although the values obtained must represent an average. This is illustrated in Figure 16, where we show the amplitude of the dominating anticyclonic motion after applying a bandpass filter, with half width points at 1.0×10^{-4} s^{-1} and 1.2×10^{-4} s^{-1}, to the spectrum of the original data set. Maximum inertial currents reach up to 8 cms^{-1}. Notice the increase of the inertial wave amplitude at the deeper current meters in the frontal zone between day 230–235 (Fig. 9). Kunze and Sanford (1984) attribute an increase in frontal, inertial energy to a trapping of inertial waves due to a local decrease in the effective Coriolis frequency (Mooers, 1975) $f_0 = f + \frac{1}{2}[(\partial v_0/\partial x) - (\partial u_0/\partial y)]$ associated with the sheared frontal jet (u_0, v_0). Also note the slow amplitude modulations in Figure 16 with a typical period of 5 days, which may not be an artifact due to the filtering procedure, but can be attributed to the beat $(\sigma - f)$ of the actual *near*-inertial frequency and the exact inertial frequency f (Gill, 1984).

Inertial motions are either directly forced by wind stress (Pollard and Millard, 1970), or appear as the transients in a geostrophic adjustment process, which, due to their low phase speeds, remain near the source (Gill, 1984).

The specific, frictionally modified, *first* mode appearance of the inertial motions is attributed to the slab-like motion of the surface layer, which is the initial response to wind forcing (Millot and Crepon, 1981). The relative forcing of the internal modes is subsequently determined by the projection of this step-function forcing on the (normal) modes, yielding a strongest forcing for the first mode.

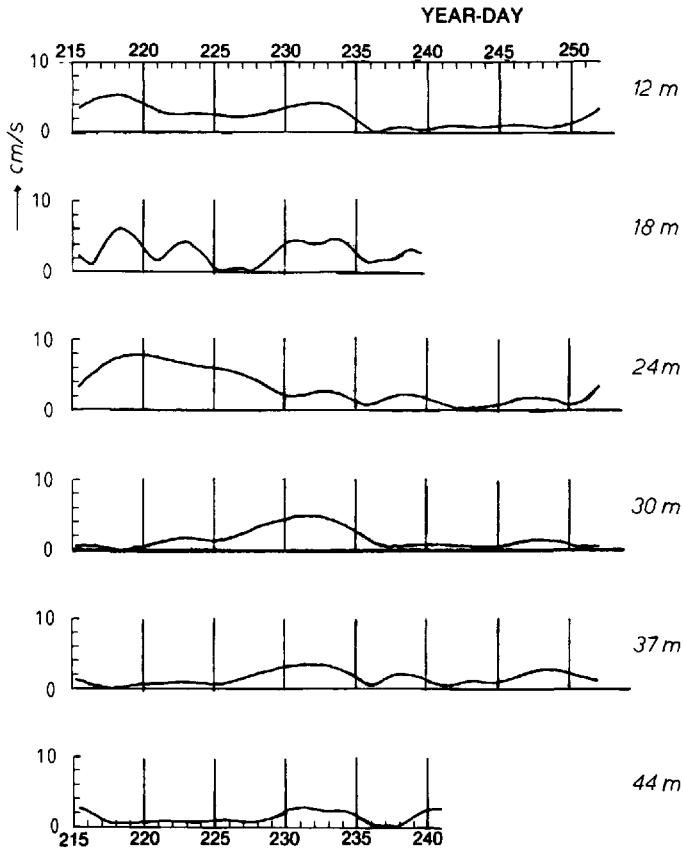

Figure 16. Slow time evolution of band-passed anticyclonic, inertial current amplitude W_- as a function of depth for position I in 1982.

5. Slow time evolution of frictional depths $\hat{\delta}_\pm$ and phase differences $\triangle\hat{\theta}_\pm$

A variation in the effective Coriolis frequency at a slow time scale should immediately be mirrored in variations in Ekman depths and total amount of phase shifts between surface and bottom currents for the semidiurnal, rotary tidal current components. For this reason we determine from the observations the slow time evolution of Ekman depths $\hat{\delta}_\pm$ and phase shifts $\triangle\hat{\theta}_\pm$ (the hat indicating the experimental determination), which are defined as the depth where the velocity obtains an (arbitrary) 0.8 value of its surface magnitude, and as the difference between phase angles at the 'surface' (θ_s) and 'bottom' current meters (θ_b) respectively. The depth $\hat{\delta}$ is set zero if the 0.8 value falls below the depth of the lowest current meter. Now since the Ekman depth $\delta = \sqrt{2K/\nu}$, it formally approaches infinity when $\nu \longrightarrow 0$, clearly a feature which cannot be simulated using the experimental definition. We therefore calculated

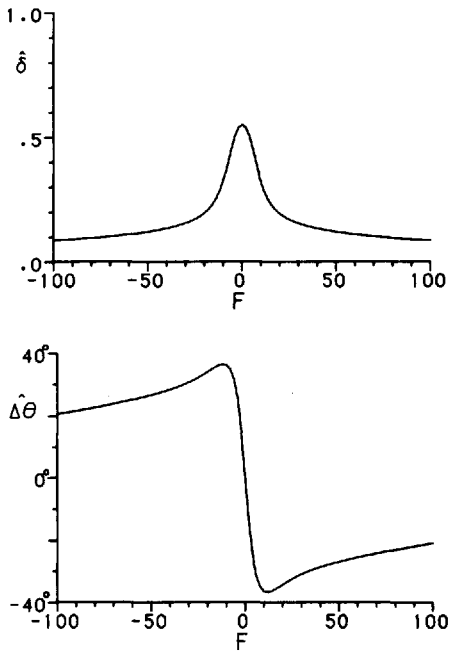

Figure 17. Profiles of $\hat{\delta}$(a) and $\triangle\hat{\theta}$(b) as a function of frequency ν scaled with the Ekman number E ($F = \nu/E$), for the theoretical Ekman solution (8).

$\hat{\delta}$ from the theoretical Ekman profile (8), with a no-slip bottom boundary condition, as a function of frame rotation rate ν, scaled by the Ekman number E (Fig. 17a). Also, since the 'bottom' current meter in the experimental setting is at an average height of $0.1 \times H$, we calculated from the Ekman solution $\triangle\hat{\theta} = \theta(1)$–$\theta(0.1)$ (Fig. 17b). Note that there exists some ambiguity in $\triangle\hat{\theta}$ values, since similar values can be obtained at different frequency ranges ν.

The observed $\hat{\delta}_\pm$ and $\triangle\hat{\theta}_\pm$ are obtained by performing a harmonic analysis over subsequent two-day periods. In view of the shortness of these periods we cannot distinguish between different semidiurnal frequencies (M_2, S_2, N_2), which are therefore lumped together. As shown in Section 4a, this has no consequence for the vertical profiles since it is the frequency σ which determines the behavior of $\hat{\delta}_\pm$ and $\triangle\hat{\theta}_\pm$.

Figure 18 shows the experimental values of these parameters for the observations in 1982 at site I. Interesting deviations from the time-averaged values (Fig. 5) occur, the most noteworthy being the unexpected high cyclonic frictional depths between day 220–230 and 235–240 (Fig. 18a). Variations in Ekman depth $\hat{\delta}_+$ for a particular frequency σ, need not necessarily be produced by changes in the effective Coriolis frequency, but may equally well result from time variations in the turbulent state of the sea. Yet, a simple increase of background turbulent eddy viscosity (e.g. due to the

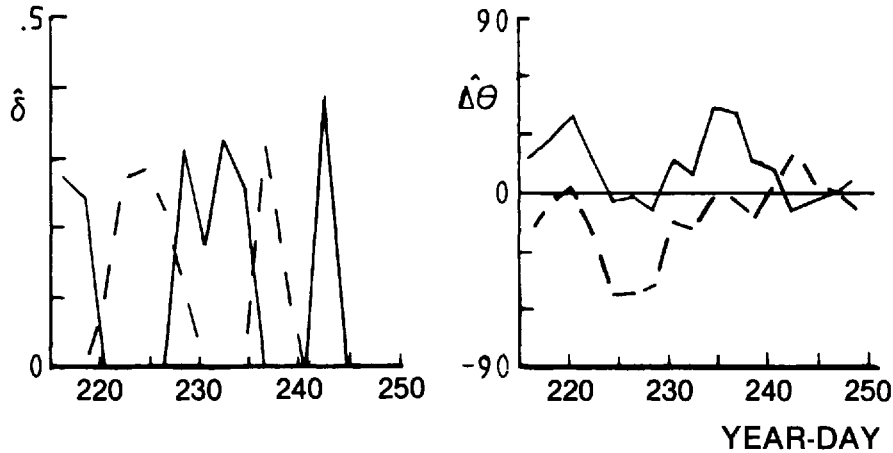

Figure 18. Slow time evolution of friction depths $\hat{\delta}_\pm$ (a) and phase differences between upper and lower current meters $\Delta\hat{\theta}_\pm$ (b) determined for the rotary current components at position I for the semidiurnal frequency band. The cyclonic component (+) is dashed; the anticyclonic component (−) is solid. Note that $\hat{\delta}$ was set zero if it was below the normalized depth of the lowest current meter.

spring-neap tidal cycle) is not a sufficient explanation, since this would correspondingly increase the anticyclonic depth $\hat{\delta}_-$. Changes in the effective Coriolis frequency, however, have opposite effects on $\hat{\delta}_+$ and $\hat{\delta}_-$, as follows from Figure 17. Sufficiently negative values of the effective Coriolis frequency may bring about a (near) resonance of the cyclonically rotating semidiurnal current component w_+ and hence explain the observed high values of $\hat{\delta}_+$. This explanation is plausible since (near) resonances of the cyclonic and anticyclonic components $\hat{\delta}_\pm$ seem to be complementary, implying a wandering of the effective Coriolis frequency in the order of $\pm f$; an unexpectedly large value (compare with oceanic values in warm-core rings, which reach magnitudes of $0.5 \times f$; Joyce and Kennelly, 1985). The observed phase differences $\Delta\hat{\theta}_\pm$ partly support this interpretation. They are not in phase with the frictional depth variations, but this is not to be expected, as we note from Figure 17, by observing how $\hat{\delta}$ and $\Delta\hat{\theta}$ vary on changes of $\nu = f_0 \pm \sigma$. Note, in Figure 18b, how, up to day 238, $\Delta\hat{\theta}_+$ follows $\Delta\hat{\theta}_-$ almost exactly. Recall that after day 240 the data become less reliable.

If the observed slow time behavior of $\hat{\delta}_\pm$ and $\Delta\hat{\theta}_\pm$ is due to variations of $O(10^{-4}\ s^{-1})$ in the effective Coriolis parameter, this implies that we must expect strong current shears at small scales (say changes of 10 cm s^{-1} over O(1 km) distances).These scales are below our observational mooring separation distances, and hence we cannot verify our suggestion directly. It would however be interesting to check the occurrence of such small-scale relative vorticity, which can possibly be ascribed to baroclinic eddies trapped to the frontal zone, whose presence is suggested in Van Aken *et al.* (1987).

6. Conclusions

The vertical structure of tidal currents can be explained physically in terms of Ekman dynamics by considering force balances in frames rotating with the net angular velocities $(f \pm \sigma)/2$, in which the rotary currents reduce to steady currents. Amplitude profiles of the rotary current components in the semidiurnal frequency band show the predicted separation in Ekman scales $\delta_\pm$ experimentally. Also, phases for these rotary current components turn in opposite (similar) directions with depth for superinertial (subinertial) motions, again in accordance with theory. The amount of agreement between observed and theoretical profiles depends on the signal-to-noise ratio of a specific tidal component. A fit of the theoretical curves to the observed vertical profiles for the M_2 frequency allows an experimental determination of an overall mean value of the vertical eddy viscosity ($K \simeq (1.4 \pm 0.1) \times 10^{-3} m^2 s^{-1}$)and drag coefficient ($C_d = (2.5 \pm 0.2) \times 10^{-3}$), of which the former is slightly less than values estimated in the literature. Near the bottom the largest deviations occur, probably because of a local decrease in eddy viscosity K, due to a decreasing mixing length. The values thus obtained are confirmed by their application to theoretical profiles at other tidal bands. For the area under consideration and the time span of typically one month, on which the observations are based, the implication is that a constant K describes the turbulence state well.

Vertical eddy viscosity variations were observed by comparing amplitude and phase variations between two short periods (15 days) having a marked difference in stratification. The stratification influence is restricted to the anticyclonic component and consists of a strong phase and amplitude jump at the bottom and interior of the pycnocline, together with an amplitude decrease in the upper layer toward the surface. The former aspect is well described using a three layer model with a smaller eddy viscosity within the pycnocline, modelling the local decrease of turbulence there. The amplitude decrease toward the surface is attributed to a small amount of stress from the air experienced by the moving water at the surface. This also suggests a negligible influence of the wind in the semidiurnal spectral band.

Inertial motions were frictionally-modified, first baroclinic mode, probably generated by the passage of storms. The small phase differences between current meters at different moorings, but with comparable depths, indicate a large wavelength. The inertial motions appear to experience some trapping in a passing front due to a local minimum in the effective Coriolis frequency; i.e. the Coriolis frequency modified by low-frequency relative vorticity.

Variations in the effective Coriolis frequency are also suggested by the vertical structure of inertial currents as well as by the experimentally determined slow time evolution of frictional depth and phase difference of the two counterrotating semidiurnal current components. Events showing large values of the cyclonic friction depth imply the presence of strong small-scale vorticity of $O(10^{-4} s^{-1})$ associated with fronts and eddies.

Acknowledgments. This study was partly performed at the Institute of Meteorology and Oceanography Utrecht, the Netherlands. The authors would like to express their gratitude to H. M. Van Aken of this institute for introducing them to the numerical aspects of tidal analysis, to H.W. Riepma of the Royal Netherlands Meteorological Institute for kindly supplying them with the current meter data records and to J. T. F. Zimmerman of the Netherlands Institute for Sea Research for his stimulating comments on an earlier draft. The valuable comments of a referee, which helped to improve our manuscript, are appreciated. The authors are supported by a grant from the Netherlands Organization for the Advancement of Pure Research (Z.W.O.).

REFERENCES

Bowden, K. F. 1983. Physical Oceanography of Coastal Waters. Ellis Horwood Limited, Chicester, 302 pp.

Csanady, G. T. 1976. Mean circulation in shallow seas. J. Geophys. Res., *81,* 5389–5399.

—— 1982. Circulation in the Coastal Ocean. D. Reidel Publishing Company, Dordrecht/Boston/London, 279 pp.

Dronkers, J. J. 1964. Tidal Computations in Rivers and Coastal Waters. North Holland Publishing Company, Amsterdam, 518 pp.

Fang, G. and T. Ichiye. 1983. On the vertical structure of tidal currents in a homogeneous sea. Geophys. J. R. Astr. Soc., *73,* 65–82.

Fjeldstad, J. E. 1963. Internal waves of tidal origin. Geof. Publik., *25,* 1–73.

Gargett, A. E. and G. Holloway. 1984. Dissipation and diffusion by internal wave breaking. J. Mar. Res., *42,* 15–27.

Gill, A. E. 1984. On the behaviour of internal waves in the wakes of storms. J. Phys. Oceanogr., *14,* 566–581.

Joyce, T. M. and M. A. Kennelly. 1985. Upper-Ocean velocity structure of Gulf Stream warm-core ring 82B. J. Geophys. Res., *90,* (C5), 8839–8844.

Kunze, E. and T. B. Sanford. 1984. Observations of near-inertial waves in a front. J. Phys. Oceanogr., *14,* 1129–1151.

Lamb, Sir H. 1975. Hydrodynamics. Cambridge University Press, Cambridge, 738 pp.

Lorentz, H. A. 1926. Verslag Staatscommissie Zuiderzee, 1916–1926, Algemene Landsdrukkerij, 's-Gravenhage, 1–345.

Millot C. and M. Crepon. 1981. Inertial oscillations on the continental shelf of the Gulf of Lions—Observations and Theory. J. Phys. Oceanogr., *11,* 639–657.

Mooers, C. N. K. 1975. Several effects of a baroclinic current on the cross-stream propagation of inertial-internal waves. Geophys. Fluid Dyn., *6,* 245–275.

Pedlosky, J. 1979. Geophysical Fluid Dynamics. Springer Verlag, New York/Heidelberg/Berlin, 624 pp.

Pollard, R. T. and R. C. Millard. 1970. Comparison between observed and simulated wind-generated inertial oscillations. Deep-Sea Res., *17,* 813–821.

Prandle, D. 1982. The vertical structure of tidal currents. Geophys. and Astrophys. Fluid Dyn., *22,* 29–49.

Schott, F. 1971. Spatial structure of inertial-period motions in a two-layered sea, based on observations. J. Mar. Res., *29,* 85–102.

—— 1977. On the energetics of baroclinic tides in the North Atlantic. Ann. Geophys., *33,* 41–62.

Soulsby, R. L. 1983. The bottom boundary layer of shelf seas, *in* Physical Oceanography of Coastal and Shelf Seas, B. Johns, ed., Elsevier Scientific Publishing Company, Amsterdam/Oxford/New York/Tokyo, 189–266.

Sverdrup, H. U. 1927. Dynamics of tides on the north Siberian Shelf. Geof. Publik., *4,* 3–75.
Tee, K.-T. 1979. The structure of three-dimensional tide generating currents. Part I, oscillating currents. J. Phys. Oceanogr., *9,* 930–944.
—— 1982. The structure of three-dimensional tide-generating currents: experimental verification of a theoretical model. Est. Coast. Shelf Sci., *14,* 27–48.
Van Aken, H. M. 1984. A one-dimensional mixed-layer model for stratified shelf seas with tide- and wind-induced mixing. Dt. Hydrogr. Z., *37,* 3–27.
—— 1986. The onset of seasonal stratification in shelf seas due to differential advection in the presence of a salinity gradient. Cont. Shelf. Res., *5,* 475–485.
Van Aken, H. M., G. J. F. van Heijst and L. R. M. Maas. 1987. Observations of fronts in the North Sea. J. Mar. Res., (in press).
Wimbush, M. and W. Munk. 1970. The benthic boundary layer, *in* The Sea, Vol. 4, Wiley, 731–758.
Wunsch, C. 1975. Internal tides. Rev. Geophys. Space Phys., *13,* 167–182.

Received: *30 July, 1986;* revised: *16 December, 1986.*